Spin-embedded diamond optomechanical resonator with a mechanical quality factor exceeding one million

Oh, H.; Darod, V.; Padgett, C.; Hughes Wyatt, L.B.; Venkatraman, J.; Parthasarathy S.; ... ; Bleszynski Jayich, A.C.

Research Article Vol. 13, No. 3 / March 2026 / Optica 485

OPTICA

Spin-embedded diamond optomechanical resonator with a mechanical quality factor exceeding one million

Hyunseok Oh,[1,†] Viraj Dharod,[1,†] Carl Padgett,[1,†] Lillian B. Hughes Wyatt,[2] Jayameenakshi Venkatraman,[1] Shreyas Parthasarathy,[1] Ekaterina Osipova,[1] Ian Hedgepeth,[1] Jeffrey V. Cady,[1] Luca Basso,[3] Yongqiang Wang,[4] Michael Titze,[5] Edward S. Bielejec,[5] Andrew M. Mounce,[3] Dirk Bouwmeester,[1,6] and Ania C. Bleszynski Jayich[1,*]

[1]Department of Physics, University of California, Santa Barbara, California 93106, USA
[2]Materials Department, University of California, Santa Barbara, California 93106, USA
[3]Center for Integrated Nanotechnologies, Sandia National Laboratories, Albuquerque, New Mexico 87123, USA
[4]Center for Integrated Nanotechnologies, Los Alamos National Laboratory, Los Alamos, New Mexico 87545, USA
[5]Sandia National Laboratories, Albuquerque, New Mexico 87185, USA
[6]Huygens-Kamerlingh Onnes Laboratory, Leiden University, P.O. Box 9504, 2300 RA Leiden, The Netherlands
[†]These authors contributed equally to this work.
*ania@physics.ucsb.edu

Received 29 August 2025; revised 26 January 2026; accepted 30 January 2026; published 10 March 2026

Diamond optomechanical crystal (OMC) devices with embedded color center spins are promising platforms for a broad range of applications in quantum sensing, networking, and computing, offering an interface between a GHz-frequency mechanical mode and both optical photons and coherent spins. A crucial but elusive step toward realizing this platform is to engineer a device with a high-quality factor mechanical mode while preserving the bulk-like coherence of embedded spins. Here, we demonstrate sideband-resolved diamond OMCs with mechanical quality factors in excess of 10^6 at cryogenic temperatures and find coherence times up to $T_2 = 227$ μs for embedded nitrogen-vacancy (NV) centers. Furthermore, we measure these devices across five orders of magnitude in intracavity optical power, demonstrating robust power handling and a high optomechanical cooperativity ($C \gg 1$) at cryogenic temperatures, which is essential for a broad range of quantum protocols requiring strong, coherent interactions between photons and phonons. These results are enabled by a robust, high-throughput method for forming single-crystal diamond membranes in combination with chemical vapor deposition (CVD) diamond overgrowth with nitrogen δ-doping. We discuss the prospects of this platform for hybrid spin-mechanical devices in the quantum regime.

https://doi.org/10.1364/OPTICA.577541

1. INTRODUCTION

Mechanical systems have risen to prominence in the fields of quantum sensing and quantum information science due to their long second-scale lifetimes [1] and demonstrated operation in the single-phonon quantum regime [2,3]. They can serve as key auxiliary components in hybrid quantum systems, offering versatile coupling to diverse quantum degrees of freedom, including photons [4], charge qubits [5], spin qubits [6], and solid-state spins [7], while maintaining high quality factors. For example, they can facilitate coupling between distant quantum systems [8] and can enable quantum information transfer across different energy scales [9,10]. Mechanical systems have great potential for quantum sensing [11–13], quantum memories [2], and quantum transduction [10,14].

Single-crystal diamond is a promising material platform for hybrid mechanical systems, featuring excellent optical, mechanical, and thermal properties [15]. Importantly, it hosts a variety of highly coherent defect-center spins, such as nitrogen-vacancy (NV) and silicon-vacancy (SiV) centers [8]. Theoretical proposals suggest the use of an engineered coupling between these localized spin-based qubits and the long-lived delocalized phononic modes of diamond mechanical oscillators for, e.g., phononic networks of defect-center spins [16], dissipative superradiant spin amplification [17], improved spin readout via an optomechanically induced transparency-assisted dispersive interaction [18], and mechanically mediated spin-spin entanglement such as two-axis twisting-induced spin squeezing via bosonic parametric driving of

an optomechanical crystal [19]. Several experiments have demonstrated strain-mediated coupling between diamond mechanical modes and embedded NV [20,21] and SiV centers [22–24].

In optomechanical devices, optical control over mechanical modes can enable, for instance, ground-state cooling [25,26] and remote quantum entanglement of mechanical oscillators [27]. A key figure of merit for accessing the quantum regime of mechanical motion in these devices is the optomechanical cooperativity, $C = \frac{4g_0^2 n_c}{\kappa \gamma_m}$, where g_0 represents the optomechanical coupling strength (i.e., the energy exchange rate between photons and phonons), κ and γ_m, respectively, denote the energy loss rates of the optical and mechanical modes, and n_c is the average number of photons in the optical cavity. In cavity optomechanics, efficient cooling to the ground state is possible with large cooperativity and in the resolved-sideband regime [25,26,28], where the mechanical resonance frequency ω_m exceeds the optical cavity linewidth κ [29].

Optomechanical crystals (OMCs), comprising photonic and phononic crystal structures on the nano- to micro-meter scale [30], host co-localized optical and mechanical modes that can be engineered with high quality factors. Due to their high mechanical frequency and amenability to optomechanical quantum control, they serve as an excellent starting point for operation in the quantum regime. Ground-state cooling [26] and entanglement of mechanical quantum states [27] have been demonstrated with GHz-frequency silicon OMCs.

The attractive features of OMCs combined with the prospect of strain-mediated coupling to embedded spins in defect-containing hosts provide strong motivation to realize spin-coupled diamond OMC devices. In recent years, there has been progress in fabricating diamond OMCs [24,31–33], though experiments are still sparse due to challenges in nanofabrication, and the demonstrated optomechanical properties have lagged their Si counterparts. One major challenge is the formation of thin films of single-crystal diamond, and several approaches have been pursued to this end. In the diamond-on-insulator (DOI) method [34,35], diamond membranes are bonded to another material and subsequently thinned to reach the target device thickness. However, the resulting membranes typically exhibit thickness variations of several microns across a mm-scale lateral extent, severely limiting the throughput of devices with a target thickness. Other techniques include top-down fabrication of bulk diamond, such as angled etching [31,33] and quasi-isotropic etching [24,36,37].

Another promising method for forming high-quality, uniform-thickness, single-crystal diamond thin films for spin-coupled diamond optomechanics involves the smart-cut technique [38], a well-established nanofabrication technique for materials beyond diamond, followed by subsequent chemical vapor deposition (CVD) diamond overgrowth [39]. The diamond smart-cut process creates a subsurface damaged layer that can be selectively removed, thus enabling the separation of a uniformly thin diamond layer from the bulk. This method has been explored for diamond optical and mechanical nanostructures [40–46] and features several advantages. The thickness uniformity enables high-throughput fabrication of nanostructures across the full diamond membrane. The rectangular cross-section, in contrast to the triangular cross-section from angled-etching approaches, eliminates the need for specialized etching techniques. Furthermore, a rectangular cross-section easily enables acoustic shielding structures around the OMC that are required for a full phononic band gap [47]. The mechanical breathing mode induces a uniform strain profile along the nanobeam thickness, permitting spins to be placed at the midpoint in depth where they are protected from surface-induced decoherence [48] and allowing for a larger uniform strain region. We note that the subsequent CVD overgrowth of high-quality diamond on smart-cut membranes is essential for good spin, optical, and mechanical properties [49].

Here, we present diamond OMC devices fabricated via the smart-cut method with high mechanical quality factors $Q_m = (1.90 \pm 0.04) \times 10^6$ and optical quality factors $Q_o = (3.781 \pm 0.004) \times 10^4$ in the resolved-sideband regime. The frequency-Q product for the 6.23 GHz mechanical mode is 1.18×10^{16} Hz. We characterize the optomechanical properties at liquid-He temperatures, demonstrating an optomechanical cooperativity of 54 measured at a large intracavity photon number $n_c = 41{,}000$ enabled by the high power-handling capability of diamond. Additionally, we measure the room-temperature spin properties of an NV center embedded within the OMC and observe a long spin coherence time of 227 μs as well as high spin-dependent optical contrast. We discuss the potential for strong mechanical coupling of these devices to embedded spins in the quantum regime.

2. DEVICE DESIGN AND FABRICATION

Our photonic/phononic cavity structure is formed by patterning elliptical holes of varying size and spacing to form cells [Fig. 1(a)]

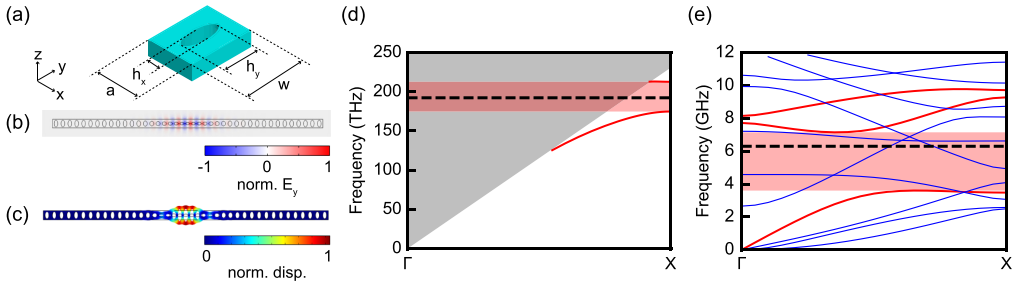

Fig. 1. Design and simulation of 1D diamond optomechanical crystal (OMC). (a) Schematic of an OMC unit mirror cell. The indicated dimensions are varied through optimization with final values $(a, w, h_x, h_y) = (650, 800, 343, 617)$ nm and nanobeam thickness $t = 250$ nm. (b) Simulated fundamental TE-like optical mode profile of the cavity resonance at $\omega_o/2\pi = 192$ THz. E_y is the normalized y-component of the electric field. (c) Simulated fundamental mechanical breathing mode profile of the cavity resonance at $\omega_m/2\pi = 6.34$ GHz. The color represents the normalized displacement field amplitude. (d) Simulated optical band structure of the unit mirror cell. The red lines correspond to the optical modes of both odd vector symmetry in the y axis and even vector symmetry in the z axis. The gray-shaded region denotes the light cone with unguided modes. (e) Simulated mechanical band structure of the unit mirror cell. The red lines are mechanical modes of even vector symmetry in both the y and z axes, while the blue lines correspond to other modes.

along the length of a 1D nanobeam. The central defect cell hosts the fundamental transverse-electric-like (TE) optical and mechanical breathing modes, while mirror cells on either side of the nanobeam host symmetry-dependent optical and mechanical quasi-bandgaps to confine the mechanical and optical modes of interest. Cells between the defect cell and the mirror cells adiabatically transition the cell geometry to minimize scattering losses. The optical and mechanical modes of our geometry are simulated using the finite element method software COMSOL, and the resulting mode profiles are shown in Figs. 1(b) and 1(c). The photonic and phononic band structure diagrams of the mirror unit cells are shown in Figs. 1(d) and 1(e), where red-shaded regions indicate quasi-bandgaps surrounding the frequencies of the optical and mechanical modes of interest, indicated by dashed black lines. The dimensions of the OMC device are chosen to optimize the optomechanical cooperativity C. We use a genetic algorithm to maximize the product $g_0 Q_o$, where g_0 and Q_o are extracted from COMSOL simulations. We note that $C \propto g_0^2 Q_o n_c \propto (g_0 Q_o)^2$ at a given laser power. The parameters are also constrained to ensure the mechanical and optical modes lie within their respective quasi-bandgaps. We do not include Q_m explicitly in the fitness function because mechanisms limiting Q_m in diamond OMCs are not yet well understood and thus difficult to capture in simulation. The simulations of the optimized OMC device geometry yield an optical resonance at $\lambda_o = 1559$ nm, a mechanical resonance at $\omega_m/2\pi = 6.34$ GHz, and $g_0/2\pi = 184$ kHz. Detailed optimization procedures are described in Section 3A of Supplement 1.

Figure 2(a) summarizes the steps for fabricating OMCs in thin-film diamond. We start with an electronic grade (100)-oriented single-crystal diamond sample (Element Six) polished to a surface roughness (R_q) of < 300 pm. A subsurface damaged layer is formed by He-ion implantation at an energy of 150 keV and a fluence of 5×10^{16} ions/cm^2, followed by graphitization upon high-temperature vacuum annealing. The result is a 400-nm-thick diamond layer atop a 100-nm-thick graphite layer. The top diamond layer is partially damaged due to the traversal of He ions, and hence to improve the device material quality, we use CVD to grow a 497-nm-thick ^{12}C isotopically purified layer with a δ-doped ^{15}N layer at a depth of 144 nm. After growth, NV centers are formed via 200 keV electron irradiation and 850°C annealing for 8 h. We next pattern 16 square membranes (400 μm × 400 μm) on the 2 × 2 mm diamond via photolithography and plasma etching. We electrochemically etch the graphite below a single target membrane in 250 mM K_2SO_4 aqueous solution with Pt wires [50] until only a small corner region of graphite tethers the diamond membrane to the substrate. Next, the diamond membrane is transferred via flip-chip bonding onto a Si carrier piece spin-coated with hydrogen silsesquioxane (HSQ) and heated to 450°C to cure the HSQ under 400 N of applied force. After HSQ curing, the bulk diamond sample is retracted from the silicon, leaving only the target membrane bonded to the Si piece. We then use $ArCl_2$ and O_2 reactive ion etching (RIE) to thin the membrane down to the target thickness of 250 nm, removing the partially He-ion-damaged diamond in the process.

We fabricate approximately 50 OMC devices on a transferred membrane [Fig. 2(b)] via e-beam lithography (EBL), followed by O_2 RIE. Each device [Fig. 2(c)] consists of an OMC nanobeam cavity, an optical waveguide for delivering light from an optical fiber to the device, and acoustic shields for suppressing clamping-induced mechanical damping. The devices are diced within a few μm of the diamond device edge to enable optical coupling to a lensed fiber with a 14 μm working distance. Detailed fabrication procedures are described in Section 1 of Supplement 1. We note that the production rate for diamond OMCs using this membrane technique is significantly higher than our previously used diamond-on-insulator (DOI) approach [32]. Many useful devices can now be fabricated on one membrane (see Section 4D of Supplement 1).

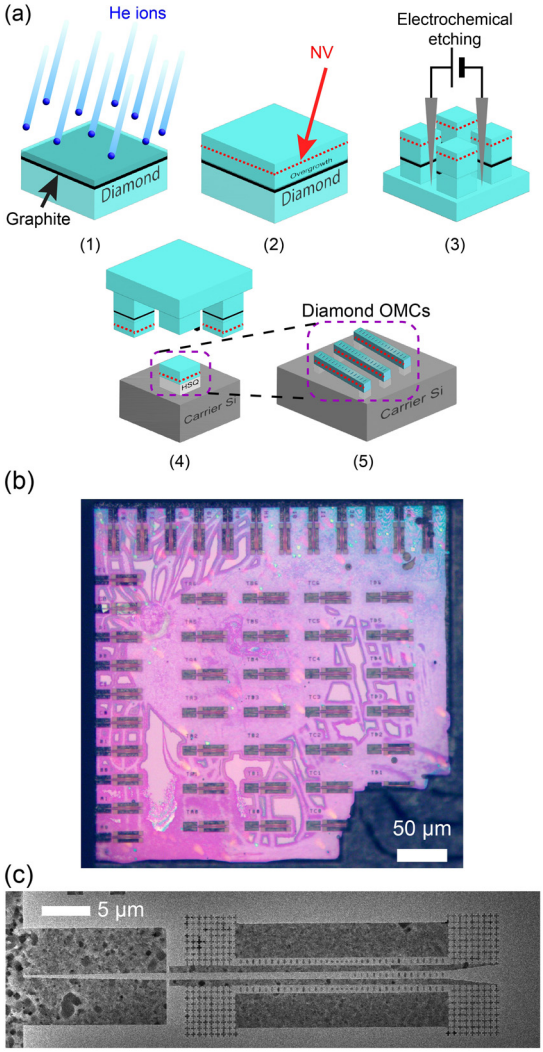

Fig. 2. (a) Steps for diamond OMC device fabrication: (1) Subsurface damage layer formation, (2) CVD diamond overgrowth with ^{15}N δ-doping, (3) electrochemical etching of patterned membranes, (4) membrane transfer to a Si carrier piece, and (5) patterning OMC devices. (b) Optical microscope image of a diamond membrane with approximately 50 fabricated OMC devices. (c) SEM image of a device, showing a pair of OMCs surrounded by acoustic shields and a tapered waveguide for optical coupling.

3. OPTOMECHANICS CHARACTERIZATION

We first present optical and mechanical spectroscopy of a diamond OMC device at cryogenic temperatures. We sweep the wavelength of a tunable external cavity diode laser to measure the optical response of the OMC [Fig. 3(a)] and extract an optical resonance wavelength of $\lambda_o = 1576.87$ nm and an optical quality factor of $Q_o = (3.781 \pm 0.004) \times 10^4$. With the laser tuned

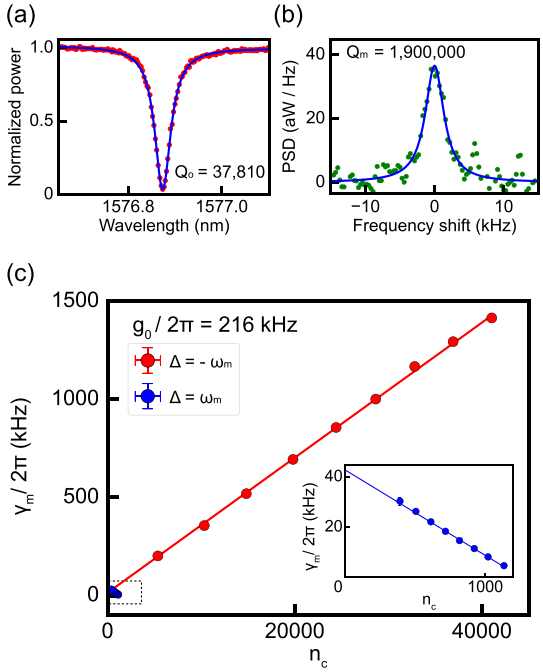

Fig. 3. (a) Optical resonance of the diamond OMC. A Fano-resonance fit (blue line) gives an optical quality factor of $(3.781 \pm 0.004) \times 10^4$. (b) Mechanical resonance of the diamond OMC at $T = 4$ K. A Lorentzian fit (blue line) gives a mechanical quality factor of $(1.90 \pm 0.04) \times 10^6$ at a center frequency of 6.23 GHz. (c) Total mechanical linewidth (γ_m) as a function of intracavity photon number (n_c) due to backaction cooling (laser on the red motional side band) and amplification (laser on the blue motional side band). The data are collected at 4K. Fitting the lines to Eq. (1) yields an optomechanical coupling strength (g_0) of 216 ± 1 kHz. Inset: Magnified blue-sideband data at low n_c.

to the red motional sideband of the OMC cavity, the mechanical Brownian motion of the cavity imprints a modulation at the mechanical frequency via optomechanical coupling. The power spectral density of the modulated tone for an intracavity photon number of $n_c = 0.27$ is shown in Fig. 3(b), from which we extract a mechanical quality factor of $Q_m = (1.90 \pm 0.04) \times 10^6$ at a sample stage temperature of 4 K. The mechanical resonance frequency is $\omega_m/2\pi = 6.23$ GHz. Measurements performed at a sample stage temperature of 160 mK yield a comparable, though slightly lower, Q_m (see Section 4C of Supplement 1). These measured parameters put our diamond OMCs in the resolved-sideband regime, with $4\omega_m/\kappa = 4.96$. We note that this is the highest Q_m reported for diamond OMC devices to date [33] and it is higher than the frequency-jitter-limited $Q_m \approx 1.31 \times 10^6$ of Si OMCs reported by MacCabe *et al.* [1], where significantly higher Q_m was also measured for the same device via ringdown measurements with short optical pulses. Future experiments will probe diamond OMCs using pulsed measurement schemes and will elucidate the origins of mechanical damping in these devices.

We characterize the optomechanical coupling between the optical and the mechanical modes by measuring the backaction-induced mechanical damping rate as a function of n_c. With a laser tuned to the red ($\Delta = -\omega_m$) or blue ($\Delta = \omega_m$) motional sideband, the total mechanical damping rate is given by

$$\gamma_m = \gamma_i \mp \frac{4g_0^2 n_c}{\kappa}\left(\frac{\left(\frac{4\omega_m}{\kappa}\right)^2}{1+\left(\frac{4\omega_m}{\kappa}\right)^2}\right), \quad \Delta = \pm\omega_m, \qquad (1)$$

where γ_m is the total mechanical damping rate, γ_i is the intrinsic mechanical damping rate, g_0 is the optomechanical coupling strength, n_c is the average number of photons in the cavity, and κ is the optical decay rate [51]. A fit to data collected at $T = 4$K [Fig. 3(c)] yields $g_0/2\pi = 214.8 \pm 0.8$ kHz on the red-sideband and $g_0/2\pi = 218 \pm 3$ kHz on the blue-sideband. At the highest measured n_c of 41,000, our device achieves an optomechanical cooperativity $C = 54 \pm 5$, demonstrating robust optical power handling. For comparison, previously reported C values for diamond OMCs range up to 19.9 [31]. We note that this cooperativity is calculated using $\gamma_i/2\pi = 28$ kHz extracted from fitting the data in Fig. 3(c) to Eq. (1). The 3.28 kHz damping rate measured in Fig. 3(b) is lower presumably due to decreased parasitic optical absorption at much lower n_c. The n_c and T dependence of Q_m will be the subject of future study. In this regime of $C \gg 1$, photons and phonons interact coherently, making diamond OMCs a promising candidate platform for e.g., ground-state cooling, quantum state transduction, and optomechanically assisted single-spin readout [18].

4. NV CENTER CHARACTERIZATION

With the goal of integrating defect-based spin qubits into optomechanical structures, it is important that the fabrication process preserves the qubit properties, leaving them as "bulk-like" as possible. The NV center is an optically addressable spin in diamond exhibiting long room-temperature quantum coherence time (T_2), and coupling its spin degree of freedom to nanoscale mechanical and optical cavities is promising for a variety of sensing and networking applications [52,53]. However, the NV center's spin and optical properties are known to be highly sensitive to nearby surfaces and proximal lattice damage induced by nanofabrication [54].

Here, we investigate NV centers inside fabricated OMCs to assess the compatibility of our fabrication process with the preservation of high-quality spin properties. We use a room-temperature confocal microscope [Fig. 4(a)] to excite the NV centers with a 532 nm laser and collect fluorescence in the 650–800 nm range with an avalanche photodiode (APD). Microwaves for driving NV spin transitions are delivered via an off-chip microwire. Figure 4(b) shows a scanning confocal image of one of our devices, where many of the bright spots correspond to fluorescent NV centers, as verified by optically detected magnetic resonance (ODMR) spectroscopy. Figure 4(c) shows Rabi oscillations of the NV spin qubit encoded in the $m_s = 0$ and $m_s = -1$ spin states; the data show an excellent spin-dependent fluorescence contrast of $\sim 31\%$, which is close to the maximum Rabi contrast typically seen for charge-stable NV centers [55]. The Rabi contrast is defined as $(PL_0 - PL_{-1})/PL_0$, where PL_0 (PL_{-1}) is the photoluminescence rate of the NV in the $m_s = 0$ ($m_s = -1$) state. Both the fluorescence rate and high contrast persist over prolonged laser illumination, indicating that the good NV charge state initialization fidelity is stable over time and robust to high light intensity. In Fig. 4(d), we plot the results of a Hahn-echo coherence time measurement and fit the data to extract $T_2 = 227 \pm 3$ μs. These results confirm the gentle nature of our diamond growth, defect incorporation, and device nanofabrication process, which preserves the charge stability and spin coherence of embedded NV centers.

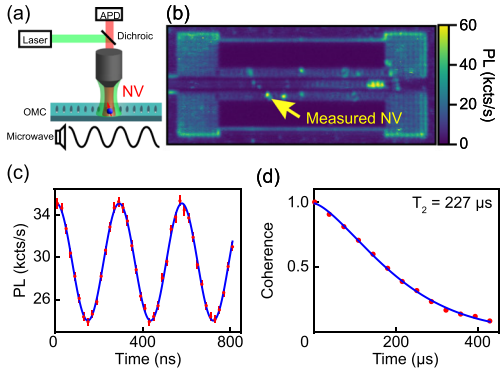

Fig. 4. Spin properties of NV centers embedded in OMCs. (a) Confocal microscopy setup. (b) Scanning confocal microscope image of an OMC device. (c) Rabi oscillations of the NV spin indicated by the yellow arrow in (b), where the NV photoluminescence (PL) oscillates as a function of the duration of an applied microwave pulse. Fitting the visibility of the Rabi fringes (the Rabi contrast) gives $31.2 \pm 0.2\%$ Rabi contrast. (d) Hahn-echo coherence decay curve for the NV indicated in (b). A stretched exponential decay fit (stretch exponent $n = 1.44 \pm 0.04$) yields $T_2 = 227 \pm 3$ μs. The coherence was sampled at times matched to the period of ^{15}N electron spin echo envelope modulation (ESEEM) to trace the decay envelope [39].

5. CONCLUSION AND OUTLOOK

The diamond OMC devices presented here exhibit high mechanical quality factors exceeding 1.9 million and optical quality factors that place them in the resolved-sideband regime. These results are enabled by a diamond smart-cut technique combined with CVD diamond overgrowth to fabricate uniformly thin nanoscale diamond membranes of high material quality. The high optomechanical cooperativity of 54 at a circulating photon number of 41,000 demonstrates a high tolerance for intracavity optical power that is promising for experiments where strong and coherent interactions between photons and phonons are required. Our devices compare favorably to state-of-the-art 1D Si OMC devices in terms of mechanical quality factors measured under continuous-wave (CW) optical probing (see Section 4E of Supplement 1) and cooperativity, for which good power handling compensates for relatively lower optomechanical coupling due to diamond's lower refractive index. We have also demonstrated optomechanical measurements at average circulating photon numbers as low as $n_c = 0.27$, a new regime for diamond optomechanical devices, enabled by a high optomechanical coupling rate. Taking the likely origin of the measured mechanical damping rate of 3.28 kHz in Fig. 3(b) to be telegraph noise stemming from interactions with local two-level systems (TLS), this represents a mechanical coherence time of 160 μs [56]. Future work involving both CW and pulsed measurements will separate the role of TLS from other mechanisms in both loss and decoherence in diamond OMCs, and also offer an opportunity to probe these TLS as contributors to surface-related noise that currently limits the sensitivity and spatial resolution of quantum sensors based on near-surface (< 10 nm depth) color centers [48]. While further study of the interplay between these devices and their thermal environment in cryogenic conditions is required for operation in the quantum regime, our measurements illustrate the aptitude of single-crystal diamond as a host for optomechanical devices and constitute a first step toward utilizing diamond OMCs as intermediaries between quantum systems, including both photons and spins.

As a platform for hybrid quantum systems, one of the key attractive features of diamond is the potential for strong mechanical coupling to embedded spins, and we next discuss the prospects for both NV center and SiV center spins in diamond OMCs. The spin–mechanical cooperativity is defined as $C_{\mathrm{sm}} = \frac{4g_{\mathrm{sm}}^2}{\gamma_{\mathrm{m}}\gamma_{\mathrm{s}}}$, where g_{sm} is the spin–mechanical coupling strength, and γ_{m} and γ_{s} are the mechanical and spin decay rates, respectively. Using FEM simulations of the mechanical mode and reported stress/strain susceptibility of the NV center [57], we estimate $g_{\mathrm{sm,NV}}/2\pi \approx 132$ Hz and $C_{\mathrm{sm,NV}} \approx 0.037$ if an NV were located in the high-strain region of our OMC device. With a longer T_2 up to 0.6 s reported at 77 K [58] enabled by dynamical decoupling at cryogenic temperatures (see Section 5 of Supplement 1 for information on the compatibility of spin-mechanical coupling with dynamical decoupling), the expected $C_{\mathrm{sm,NV}}$ increases to ≈ 77. The prospects are significantly improved for the SiV center, which exhibits larger strain susceptibility than the NV center due to its strong strain-orbit coupling and different orbital character of the ground and excited spin qubit states [22]. For an SiV center, $g_{\mathrm{sm,SiV}}/2\pi$ reaches 8 MHz at 3.3 T and asymptotically approaches 9 MHz in the limit of high magnetic field, and the predicted $C_{\mathrm{sm,SiV}}$ exceeds 10^9 with the reported $T_2 = 13$ ms at 100 mK [59].

Funding. National Science Foundation (OMA-2016245, DMR-1906325, DMR-2308708, CNS-1725797, 2137740); The Netherlands Organisation for Scientific Research (024.003.037); Eddleman Quantum Institute.

Acknowledgment. We gratefully acknowledge support from the NSF QLCI program through Grant No. OMA-2016245, as well as the use of shared facilities of the UCSB Quantum Foundry through the Q-AMASE-i program (NSF DMR-1906325), the UCSB MRSEC (NSF DMR-2308708), and the Center for Scientific Computing (CSC) (NSF CNS-1725797). This work was performed, in part, in the UCSB Nanofabrication Facility, an open access laboratory and at the Center for Integrated Nanotechnologies, U.S. Department of Energy's Office of Science User Facility jointly operated by Los Alamos and Sandia National Laboratories. We particularly thank Demis John for help with the fabrication process development. C. P., L. B. H, and I. H. acknowledge support from the UCSB Quantum Foundry, and H.O. and V. D. acknowledge support from the Eddleman Quantum Institute. D. B. acknowledges support from NSF Award No. 2137740 and NWO Grant No. 024.003.037.

Disclosures. The authors declare no conflicts of interest.

Data availability. Data underlying the results presented in this paper are not publicly available at this time but may be obtained from the authors upon reasonable request.

Supplemental document. See Supplement 1 for supporting content.

REFERENCES

1. G. S. MacCabe, H. Ren, J. Luo, *et al.*, "Nano-acoustic resonator with ultralong phonon lifetime," Science **370**, 840–843 (2020).
2. A. Wallucks, I. Marinković, B. Hensen, *et al.*, "A quantum memory at telecom wavelengths," Nat. Phys. **16**, 772–777 (2020).
3. E. A. Wollack, A. Y. Cleland, R. G. Gruenke, *et al.*, "Quantum state preparation and tomography of entangled mechanical resonators," Nature **604**, 463–467 (2022).
4. P. F. Cohadon, A. Heidmann, and M. Pinard, "Cooling of a mirror by radiation pressure," Phys. Rev. Lett. **83**, 3174–3177 (1999).
5. M. D. LaHaye, J. Suh, P. M. Echternach, *et al.*, "Nanomechanical measurements of a superconducting qubit," Nature **459**, 960–964 (2009).
6. D. Rugar, R. Budakian, H. J. Mamin, *et al.*, "Single spin detection by magnetic resonance force microscopy," Nature **430**, 329–332 (2004).
7. E. R. MacQuarrie, T. A. Gosavi, N. R. Jungwirth, *et al.*, "Mechanical spin control of nitrogen-vacancy centers in diamond," Phys. Rev. Lett. **111**, 227602 (2013).
8. D. Lee, K. W. Lee, J. V. Cady, *et al.*, "Topical review: spins and mechanics in diamond," J. Opt. **19**, 033001 (2017).

9. R. W. Andrews, R. W. Peterson, T. P. Purdy, *et al.*, "Bidirectional and efficient conversion between microwave and optical light," Nat. Phys. **10**, 321–326 (2014).
10. M. Mirhosseini, A. Sipahigil, M. Kalaee, *et al.*, "Superconducting qubit to optical photon transduction," Nature **588**, 599–603 (2020).
11. T. P. Purdy, P.-L. Yu, R. W. Peterson, *et al.*, "Strong optomechanical squeezing of light," Phys. Rev. X **3**, 031012 (2013).
12. A. Kronwald, F. Marquardt, and A. A. Clerk, "Arbitrarily large steady-state bosonic squeezing via dissipation," Phys. Rev. A **88**, 063833 (2013).
13. E. E. Wollman, C. U. Lei, A. J. Weinstein, *et al.*, "Quantum squeezing of motion in a mechanical resonator," Science **349**, 952–955 (2015).
14. A. Bienfait, K. J. Satzinger, Y. P. Zhong, *et al.*, "Phonon-mediated quantum state transfer and remote qubit entanglement," Science **364**, 368–371 (2019).
15. S. E. Coe and R. S. Sussmann, "Optical, thermal and mechanical properties of CVD diamond," Diam. Relat. Mater. **9**, 1726–1729 (2000).
16. S. J. M. Habraken, K. Stannigel, M. D. Lukin, *et al.*, "Continuous mode cooling and phonon routers for phononic quantum networks," New J. Phys. **14**, 115004 (2012).
17. M. Koppenhöfer, P. Groszkowski, H.-K. Lau, *et al.*, "Dissipative superradiant spin amplifier for enhanced quantum sensing," PRX Quantum **3**, 030330 (2022).
18. M. Koppenhöfer, C. Padgett, J. V. Cady, *et al.*, "Single-spin readout and quantum sensing using optomechanically induced transparency," Phys. Rev. Lett. **130**, 093603 (2023).
19. P. Groszkowski, H.-K. Lau, C. Leroux, *et al.*, "Heisenberg-limited spin squeezing via bosonic parametric driving," Phys. Rev. Lett. **125**, 203601 (2020).
20. P. Ovartchaiyapong, K. W. Lee, B. A. Myers, *et al.*, "Dynamic strain-mediated coupling of a single diamond spin to a mechanical resonator," Nat. Commun. **5**, 4429 (2014).
21. K. W. Lee, D. Lee, P. Ovartchaiyapong, *et al.*, "Strain coupling of a mechanical resonator to a single quantum emitter in diamond," Phys. Rev. Appl. **6**, 034005 (2016).
22. S. Meesala, Y.-I. Sohn, B. Pingault, *et al.*, "Strain engineering of the silicon-vacancy center in diamond," Phys. Rev. B **97**, 205444 (2018).
23. S. Maity, L. Shao, S. Bogdanović, *et al.*, "Coherent acoustic control of a single silicon vacancy spin in diamond," Nat. Commun. **11**, 193 (2020).
24. G. Joe, M. Haas, K. Kuruma, *et al.*, "Observation of the acoustic Purcell effect with a color-center and a nanomechanical resonator," arXiv (2025).
25. J. D. Teufel, T. Donner, D. Li, *et al.*, "Sideband cooling of micromechanical motion to the quantum ground state," Nature **475**, 359–363 (2011).
26. J. Chan, T. P. M. Alegre, A. H. Safavi-Naeini, *et al.*, "Laser cooling of a nanomechanical oscillator into its quantum ground state," Nature **478**, 89–92 (2011).
27. R. Riedinger, A. Wallucks, I. Marinković, *et al.*, "Remote quantum entanglement between two micromechanical oscillators," Nature **556**, 473–477 (2018).
28. A. Schliesser, R. Rivière, G. Anetsberger, *et al.*, "Resolved-sideband cooling of a micromechanical oscillator," Nat. Phys. **4**, 415–419 (2008).
29. F. Marquardt, J. P. Chen, A. A. Clerk, *et al.*, "Quantum theory of cavity-assisted sideband cooling of mechanical motion," Phys. Rev. Lett. **99**, 093902 (2007).
30. M. Eichenfield, J. Chan, R. M. Camacho, *et al.*, "Optomechanical crystals," Nature **462**, 78–82 (2009).
31. M. J. Burek, J. D. Cohen, S. M. Meenehan, *et al.*, "Diamond optomechanical crystals," Optica **3**, 1404–1411 (2016).
32. J. V. Cady, O. Michel, K. W. Lee, *et al.*, "Diamond optomechanical crystals with embedded nitrogen-vacancy centers," Quantum Sci. Technol. **4**, 024009 (2019).
33. G. Joe, C. Chia, B. Pingault, *et al.*, "High Q-factor diamond optomechanical resonators with silicon vacancy centers at millikelvin temperatures," Nano Lett. **24**, 6831–6837 (2024).
34. P. Ovartchaiyapong, L. M. A. Pascal, B. A. Myers, *et al.*, "High quality factor single-crystal diamond mechanical resonators," Appl. Phys. Lett. **101**, 163505 (2012).
35. Y. Tao, J. M. Boss, B. A. Moores, *et al.*, "Single-crystal diamond nanomechanical resonators with quality factors exceeding one million," Nat. Commun. **5**, 3638 (2014).
36. B. Khanaliloo, M. Mitchell, A. C. Hryciw, *et al.*, "High-Q/V monolithic diamond microdisks fabricated with quasi-isotropic etching," Nano Lett. **15**, 5131–5136 (2015).
37. M. Mitchell, D. P. Lake, and P. E. Barclay, "Realizing Q> 300 000 in diamond microdisks for optomechanics via etch optimization," APL Photonics **4**, 016101 (2019).
38. M. Bruel, B. Aspar, B. Charlet, *et al.*, "'Smart cut': a promising new SOI material technology," in *IEEE International SOI Conference Proceedings* (1995), pp. 178–179.
39. K. Ohno, F. J. Heremans, L. C. Bassett, *et al.*, "Engineering shallow spins in diamond with nitrogen delta-doping," Appl. Phys. Lett. **101**, 082413 (2012).
40. B. A. Fairchild, P. Olivero, S. Rubanov, *et al.*, "Fabrication of ultrathin single-crystal diamond membranes," Adv. Mater. **20**, 4793–4798 (2008).
41. J. C. Lee, A. P. Magyar, D. O. Bracher, *et al.*, "Fabrication of thin diamond membranes for photonic applications," Diam. Relat. Mater. **33**, 45–48 (2013).
42. A. H. Piracha, K. Ganesan, D. W. M. Lau, *et al.*, "Scalable fabrication of high-quality, ultra-thin single crystal diamond membrane windows," Nanoscale **8**, 6860–6865 (2016).
43. X. Guo, N. Delegan, J. C. Karsch, *et al.*, "Tunable and transferable diamond membranes for integrated quantum technologies," Nano Lett. **21**, 10392–10399 (2021).
44. X. Guo, M. Xie, A. Addhya, *et al.*, "Direct-bonded diamond membranes for heterogeneous quantum and electronic technologies," Nat. Commun. **15**, 8788 (2024).
45. S. W. Ding, M. Haas, X. Guo, *et al.*, "High-Q cavity interface for color centers in thin film diamond," Nat. Commun. **15**, 6358 (2024).
46. L. Basso, M. Titze, J. Henshaw, *et al.*, "Fabrication of thin diamond membranes by Ne+ implantation," Giant **17**, 100238 (2024).
47. J. Chan, A. H. Safavi-Naeini, J. T. Hill, *et al.*, "Optimized optomechanical crystal cavity with acoustic radiation shield," Appl. Phys. Lett. **101**, 081115 (2012).
48. B. A. Myers, A. Das, M. C. Dartiailh, *et al.*, "Probing surface noise with depth-calibrated spins in diamond," Phys. Rev. Lett. **113**, 027602 (2014).
49. J. C. Lee, D. O. Bracher, S. Cui, *et al.*, "Deterministic coupling of delta-doped nitrogen vacancy centers to a nanobeam photonic crystal cavity," Appl. Phys. Lett. **105**, 261101 (2014).
50. J. J. Tully, E. Braxton, S. J. Cobb, *et al.*, "Diamond membrane production: the critical role of radicals in the non-contact electrochemical etching of sp2 carbon," Carbon **185**, 717–726 (2021).
51. M. Aspelmeyer, T. J. Kippenberg, and F. Marquardt, "Cavity optomechanics," Rev. Mod. Phys. **86**, 1391–1452 (2014).
52. K. Jensen, N. Leefer, A. Jarmola, *et al.*, "Cavity-enhanced room-temperature magnetometry using absorption by nitrogen-vacancy centers in diamond," Phys. Rev. Lett. **112**, 160802 (2014).
53. H. Kaupp, T. Hümmer, M. Mader, *et al.*, "Purcell-enhanced single-photon emission from nitrogen-vacancy centers coupled to a tunable microcavity," Phys. Rev. Appl. **6**, 054010 (2016).
54. L. V. H. Rodgers, L. B. Hughes, M. Xie, *et al.*, "Materials challenges for quantum technologies based on color centers in diamond," MRS Bull. **46**(7), 623–633 (2021).
55. Z. Yuan, M. Fitzpatrick, L. V. H. Rodgers, *et al.*, "Charge state dynamics and optically detected electron spin resonance contrast of shallow nitrogen-vacancy centers in diamond," Phys. Rev. Res. **2**, 033263 (2020).
56. P. J. J. O'Malley, "Superconducting qubits: dephasing and quantum chemistry," Ph.D. thesis (UC Santa Barbara, 2016).
57. A. Barfuss, M. Kasperczyk, J. Kölbl, *et al.*, "Spin-stress and spin-strain coupling in diamond-based hybrid spin oscillator systems," Phys. Rev. B **99**, 174102 (2019).
58. N. Bar-Gill, L. M. Pham, A. Jarmola, *et al.*, "Solid-state electronic spin coherence time approaching one second," Nat. Commun. **4**, 1743 (2013).
59. D. D. Sukachev, A. Sipahigil, C. T. Nguyen, *et al.*, "Silicon-vacancy spin qubit in diamond: a quantum memory exceeding 10 ms with single-shot state readout," Phys. Rev. Lett. **119**, 223602 (2017).